Cryo-electron tomography on focused ion beam lamellae transforms structural cell biology

nature methods

Review article

https://doi.org/10.1038/s41592-023-01783-5

Cryo-electron tomography on focused ion beam lamellae transforms structural cell biology

Received: 7 May 2021

Accepted: 20 January 2023

Published online: 13 March 2023

Check for updates

Casper Berger[1,2], Navya Premaraj[1], Raimond B. G. Ravelli[1], Kèvin Knoops[1], Carmen López-Iglesias[1] & Peter J. Peters[1]

Cryogenic electron microscopy and data processing enable the determination of structures of isolated macromolecules to near-atomic resolution. However, these data do not provide structural information in the cellular environment where macromolecules perform their native functions, and vital molecular interactions can be lost during the isolation process. Cryogenic focused ion beam (FIB) fabrication generates thin lamellae of cellular samples and tissues, enabling structural studies on the near-native cellular interior and its surroundings by cryogenic electron tomography (cryo-ET). Cellular cryo-ET benefits from the technological developments in electron microscopes, detectors and data processing, and more in situ structures are being obtained and at increasingly higher resolution. In this Review, we discuss recent studies employing cryo-ET on FIB-generated lamellae and the technological developments in ultrarapid sample freezing, FIB fabrication of lamellae, tomography, data processing and correlative light and electron microscopy that have enabled these studies. Finally, we explore the future of cryo-ET in terms of both methods development and biological application.

Macromolecules are essential to life. Determining their structure is crucial to understand how they perform their myriad biological functions. Recent advances in cryogenic electron microscopy (cryo-EM)—also known as the resolution revolution[1]—have made it possible to routinely achieve structures of isolated proteins and other macromolecules at near-atomic, and even atomic, resolution[2,3]. However, isolating macromolecules from their biological context can be challenging, or even impossible. More importantly, macromolecular conformations and functions are deeply rooted in their cellular context, and isolating macromolecules from their native surroundings can disrupt intricate interaction networks and change macromolecular structure. It is therefore essential to study macromolecules in their unperturbed cellular environment, to understand their function and conformational landscape in relation to interaction partners, cellular location and the physiological state of the cell.

Recent advances in cellular cryogenic electron tomography (cryo-ET) allow scientists to perform these critical studies. To preserve the fine molecular details of the cell in a near-native state, cells, tissues or small organisms are first frozen within milliseconds to at least below −150 °C (ref. [4]). Next, a cryo-ET instrument is used to acquire images at different tilt angles, which are subsequently used to reconstruct a volume of the sample to provide three-dimensional (3D) data on cells under near-native conditions. This can be done directly on thin samples (<500 nm) such as thin bacteria and the edges of mammalian cells[5,6]. Macromolecular structures can be determined from these data by subtomogram averaging, where hundreds to many thousands of 3D images are iteratively aligned and averaged[7,8].

However, most biological samples are thicker than 500 nm, and two techniques have been developed to generate thin biological samples while maintaining their vitreous state: cryogenic sectioning

[1]Division of Nanoscopy, Maastricht MultiModal Molecular Imaging Institute, Maastricht University, Maastricht, the Netherlands. [2]Present address: Structural Biology, The Rosalind Franklin Institute, Didcot, UK. e-mail: pj.peters@maastrichtuniversity.nl

and cryogenic focused ion beam (cryo-FIB) milling. Cryogenic sectioning uses a diamond knife to prepare <70 nm sections of cellular material[9,10], but causes several artifacts, including severe compression in the cutting direction (Fig. 1a–c) and wrinkling of the sections[11]. As an alternative to cryogenic sectioning, cryo-FIB milling causes fewer artifacts (for example curtaining or redeposition), most of which can be avoided[12–15] (Fig. 1d–l). The cryo-FIB milling process and its artifacts are explained in detail in refs. [14,15].

FIB fabrication of lamellae originated from materials science, and pioneering experiments established the proof of principle that it can also be applied under cryogenic conditions to frozen biological samples without devitrifying them[12,16–19]. FIB fabrication removes all of the material above and below a section of the cell (Fig. 1e–h), leaving a thin (50–300 nm local thickness) slice of cellular material, termed a lamella. More recently, cryo-ET imaging on FIB-fabricated lamellae has been used to successfully study the molecular environment of the cell[20,21] and is now rapidly evolving into a powerful in situ structural imaging technique.

This Review explores the unique strengths and weaknesses of cryo-ET on FIB-fabricated lamellae and which types of research questions it can answer by describing recent studies that use these techniques. Next, we outline the most recent advances in FIB preparation of lamellae, cryo-ET, data processing and subtomogram averaging that have made these studies possible. We then discuss the challenges in finding macromolecules of interest in the crowded cellular environment, and the role and potential of correlative light and electron microscopy (CLEM) for FIB-fabricated lamellae. Finally, we discuss the future potential of cryo-ET for in situ structural biology and which advances would facilitate its realization.

In situ structural studies of the cell by cryo-ET on FIB-fabricated lamellae

Cellular cryo-ET has several key advantages over other structural techniques, stemming from observing macromolecules within their native cellular environment. Besides structural findings, high-resolution imaging of the near-native cellular environment allows for visualizing cellular morphology in close detail.

Determining structures within the cell

Numerous atomic models of biomolecules based on high-resolution experimental data have been determined using structural techniques such as X-ray crystallography, single-particle cryo-EM and NMR. Cryo-ET on FIB-fabricated lamellae can complement these structural data in the near-native cellular environment, where all natively present (macro) molecular interactions are retained. This advantage makes cryo-ET a powerful method with which to validate (near-)atomic-resolution structures of isolated macromolecules obtained using other structural techniques. An example is the coat structure of coat protein complex I-coated vesicles, where cryo-ET on FIB-fabricated lamellae was used to validate a previously determined structure obtained on reconstituted vesicles[22,23]. Compared with in vitro reconstituted vesicles, the intracellular view uniquely shows their native architecture and the relative abundance of the coated and uncoated states, which provides insight about the relative half-life of coat protein complex I-coated vesicles[22]. Another example is the in situ structure of the proteinaceous shell formed around the replicative compartment of jumbo phages during infection of bacteria[24]. An intracellular subtomogram-averaged structure of the shell protein chimallin was limited to 24 Å, due to the variable curvatures and heterogenous nature of the shell. By fitting the 3.1 Å single-particle structure of the isolated chimalin monomer into the subtomogram averaging map, the higher-order native assembly of the chimalin shell could be determined, revealing a flexible geometry that can accommodate the variable curvatures of the replicate compartment.

Other examples of in situ structures include the transmembrane ribosome–translocon complex bound to the endoplasmic reticulum[25,26]; the retromer coat in algae[27]; the nuclear pore complex in algae, yeast and human cells[28–30]; the calcium channel CatSper in sperm flagella[31]; the centriole in algae[32]; the severe acute respiratory syndrome coronavirus 2 (SARS-CoV-2) spike protein during intracellular infection[33]; and the bacterial type III secretion system during intracellular infection of primary immune cells[34].

Although most structures currently obtained with subtomogram averaging on lamellae have a resolution of between 1 and 4 nm, several recent studies have obtained structures at subnanometer resolution[35,36]. In two studies by Wang et al.[37,38], structures were obtained of the thin and thick filaments in sarcomeres in muscle tissue, including that of nebulin bound to actin–myosin complexes at 5–10 Å resolution (Fig. 2a). Importantly, the structure of the molecular ruler nebulin was found to be very different within tissue compared with isolated structures, and different structural states were observed for the double heads of the molecular motor protein myosin.

Visualizing the native cellular environment may also lead to the discovery of new binding partners[39,40], or even unknown macromolecular complexes and structures. An example is the discovery of a coronavirus pore structure formed by the murine hepatitis virus (MHV) in FIB-fabricated lamellae of infected mammalian cells (Fig. 2b)[40]. This pore structure spans the double membrane of the MHV replication compartments, termed double-membrane vesicles, and may function as a transport gate for viral RNA to enter the cytosol. These molecular pores were also confirmed to be formed by SARS-CoV-2 in samples chemically fixed before ultrarapid freezing. Other examples of novel structures identified with cryo-ET on FIB-fabricated lamella include transmembrane nanobristles on intestinal microvilli in *Caenorhabditis elegans*[41] and a dome-shaped protein complex with a still unknown function on the outer membranes of lamellar bodies in primary human small airway epithelial cells[42]. Knockout mutants[39] or fusion proteins[40] can be used to confirm the identity of proteins. To understand macromolecular structures in relation to function or disease, cellular stimuli and mutants can be used. For example, Weiss and colleagues[39] applied cell stress stimuli before ultrarapid freezing of cyanobacteria to determine the structure of a novel protein complex termed septal junctions, in both open and closed conformations, using cryo-ET on FIB-fabricated lamellae. These junctions connect neighboring cells similarly to gap junctions in mammals.

Mapping structural heterogeneity within the cell

Macromolecular structures are seldom static and may change depending on subcellular localization or binding partners. Thus, determining the structures of macromolecular complexes within the cell allows the subcellular localization and spacing of macromolecules relative to one another and to organelles to be preserved. Cryo-ET on FIB-fabricated lamellae can be used to create a visual map of macromolecules in different conformational states by combining automated detection of macromolecules (for example, template matching) with subtomogram averaging and classification. Macromolecule identity, orientation, structural state and binding partners can be determined and mapped back into the tomographic volume. In this way, structural information is combined with macromolecular spatial organization and subcellular localization[20,43]. Combining structural states, macromolecular orientation and subcellular position to create a molecular atlas of the whole proteome has been termed visual proteomics[43]. Currently, subtomogram averaging is limited to macromolecules that are a part of larger macromolecular complexes (>300 kDa or thereabouts), because their coordinates in tomograms need to be (visually) determined (as discussed in the section 'Interpreting tomograms of the crowded cellular environment'). This limitation greatly restricts the fraction of the proteome that can be structurally analyzed with subtomogram averaging and subsequently mapped back into the tomographic volume. Recent examples of studies that effectively combine structural information and subcellular distribution with molecular mapping are those of Albert et al.[44,45], which looked at the structural heterogeneity

https://doi.org/10.1038/s41592-023-01783-5

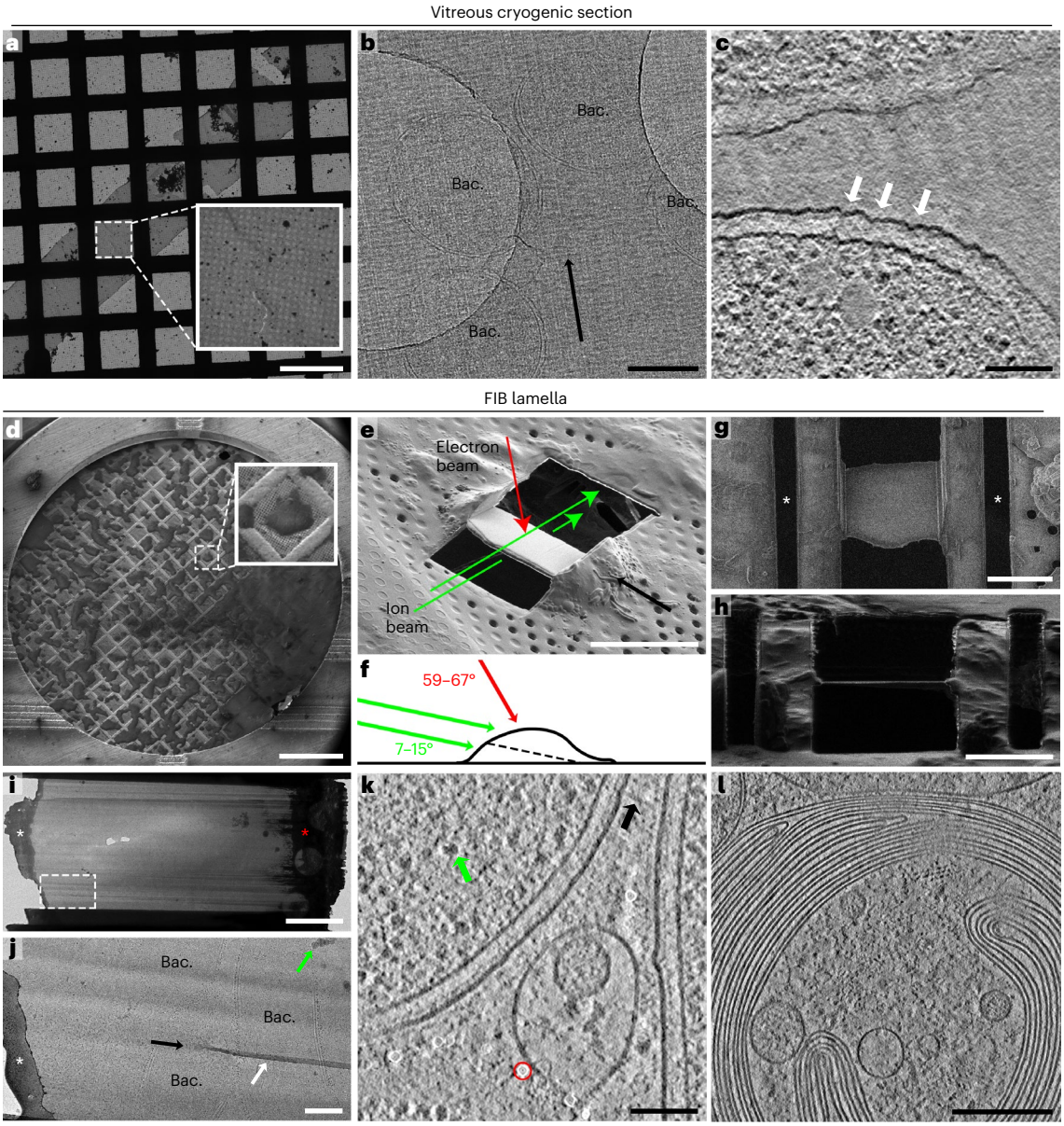

Fig. 1 | Overview of vitreous cryogenic sectioning and FIB fabrication of lamellae. a, TEM low-magnification overview of a vitreous cryogenic section of high-pressure-frozen bacteria (*Yersinia enterocolitica*) on a holey carbon electron microscopy grid. Scale bar, 150 µm. **b**, Intermediate-magnification low-dose TEM overview of a vitreous cryogenic section. Knife marks created during the sectioning can be seen as parallel lines that run in the cutting direction of the diamond knife (black arrow). Several bacteria (Bac.) are visible in the holes and on the carbon. Scale bar, 500 nm. **c**, Tomographic slice recorded on a vitreous section of high-pressure-frozen *Y. enterocolitica*. Deformations of the bacterial membrane are visible (white arrows), which are common artifacts caused by vitreous sectioning. Scale bar, 100 nm. **d**, SEM overview of an electron microscopy grid with adherent dendritic cells infected with *Y. enterocolitica*, used to select cells suitable for FIB fabrication of lamellae. The enlarged area shows a cluster of cells suitable for FIB milling. Scale bar, 500 µm. **e**, FIB image of a lamella of ~1 µm thickness during the FIB fabrication process. All of the cellular material above and below a section of the cell is removed with the FIB at a shallow angle relative to the grid with increasingly lower ion beam currents, ultimately retaining a 50–300 nm thin lamella. The approximate directions of the ion and electron beam are indicated with arrows (green and red, respectively). The black arrow indicates the approximate viewing direction in **f**. Scale bar, 20 µm. **f**, Schematic side view of FIB milling geometry on a cell on a grid. The angles of the FIB and the SEM beam are indicated in green and red, respectively. The dashed line in the cell indicates where the lamella is formed after FIB milling. **g**, SEM image of the final ~200 nm thin lamella. Micro-expansion joints[69] are visible on both sides of the lamella (as indicated by asterisks), which are formed with the FIB to prevent the lamella from cracking due to a build up of tension in the grid foil. Scale bar, 10 µm. **h**, FIB image of the lamella in **g** from the direction of the FIB during lamella fabrication. Scale bar, 10 µm. **i**, Low-dose stitched tilescan TEM overview of a lamella used to select positions for recording tilt series. The image shows the gold grid foil (red asterisk) and an organometallic platinum layer to protect the front edge from the ion beam (white asterisk). Scale bar, 5 µm. **j**, Enlarged area of the white dashed box in **i**. Several intracellular bacteria are visible. Uneven milling speeds, caused by differences in local densities of the cell, can create streak artifacts in the direction of the ion beam (black arrow) known as curtaining (white arrow). Ice contamination is indicated with a green arrow. Scale bar, 500 nm. **k**, Tomographic slice recorded on a FIB-fabricated lamella of *Y. enterocolitica* during intracellular infection of a dendritic cell. Several different macromolecule complexes are visible, including the needle of the bacterial type III secretion system (black arrow) and ribosomes (green arrow). 10 nm nanogold fiducials, used for tilt-series alignment, were computationally subtracted from the tomogram (red circle). Scale bar, 100 nm. **l**, Tomographic slice of a major histocompatibility complex class II compartment recorded on a FIB-fabricated lamella of a primary human dendritic cell. Scale bar, 200 nm.

https://doi.org/10.1038/s41592-023-01783-5

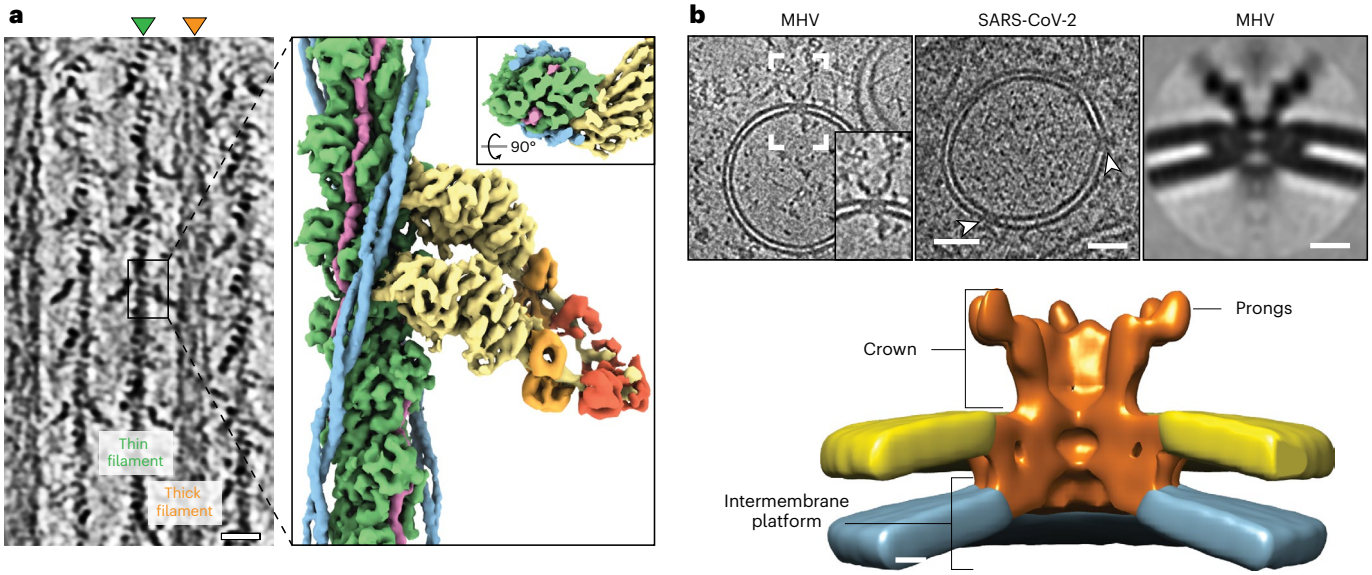

Fig. 2 | Examples of structures obtained within cells with cryo-ET on FIB-fabricated lamellae and subsequent subtomogram averaging. a, Left, tomographic slice of a sarcomere A band from skeletal mouse muscle tissue, obtained with cryo-ET on a cryo-FIB-fabricated lamella. Thin actin and thick myosin filaments are readily visible, as well as myosin double heads. Scale bar, 20 nm. Right, density map of the thin filaments obtained with subtomograms, averaging at a resolution of 5–7 Å. This density map enabled structural analysis of the structures of actin (green), tropomyosin (blue) and nebulin (magenta), as well as the structure of myosin double heads (heavy chain, yellow; essential light chain, orange; regulatory light chain, red). Adapted with permission from ref. [38], AAAS. **b**, Structure of the coronavirus pore complex in mammalian cells. Top left and middle, 7-nm-thick tomographic slices of double-membrane vesicles (DMV) formed by MHV and SARS-CoV-2, respectively. Pore complexes formed by coronaviruses span the DMV membranes (white arrowheads and inset on top right) and are probably involved in transporting viral RNA into the cytosol of the host cell. Scale bars, 50 nm. Top right, central slice of the subtomogram average of the pore complex from tomograms on FIB-fabricated lamellae of cells infected with MHV. Scale bar, 10 nm. Bottom, isosurface rendering of the subtomogram-averaged structure of the pore complex (orange) spanning the inner and outer DMV membranes (blue and yellow, respectively). The pore structure has a sixfold rotational symmetry and a central channel with a minimum diameter of ~2–3 nm. Adapted with permission from ref. [40], AAAS.

of the proteasome in algae relative to its subcellular location. They identified three distinct subpopulations based on their subcellular location: proteasomes tethered to the nuclear envelope, proteasomes tethered to the basket of the nuclear pore complex and proteasomes localized in clusters near the endoplasmic reticulum. Those of the last group are more often in the active state and contain additional densities, which the authors conclude are protein substrates from the endoplasmic reticulum that are degraded by the proteasomes[45]. In a similar study, Guo et al.[46] identified a local increase of proteasomes around poly-GA aggregates in primary rat neurons, which are more often in a stalled conformation.

Cellular ultrastructure

Besides structural information on macromolecules, cryo-ET on FIB-fabricated lamellae provides data on cellular morphology at nanometer resolution and allows for small ultrastructural features to be studied in a near-native state at a resolution currently not yet feasible with other cellular imaging techniques such as serial FIB scanning electron microscopy (SEM) imaging[47]. An example is the recent study on the effect of several cortical endoplasmic reticulum–plasma membrane tethers on endoplasmic reticulum membrane morphology[48]. The authors identified that the proteins tricalbin 1–3 are responsible for forming sharp cortical endoplasmic reticulum membrane curvatures of ~15 nm facing the plasma membrane. These areas were found to be involved in protecting the cell against heat shock, presumably by allowing transfer of lipids from the cortical endoplasmic reticulum to the plasma membrane. The morphology of the endoplasmic reticulum–plasma membrane contact sites formed by these tethers is difficult to study with classical electron microscopy methods, which can change the membrane morphology. Khanna et al.[49] observed nanometer-sized morphological changes in the peptidoglycan layer of *Bacillus subtilis* during early sporulation: by blocking peptidoglycan synthesis with antibiotics during sporulation, they found that the peptidoglycan layer was not fully degraded at the start of engulfment.

Other examples of cryo-ET on FIB-fabricated lamellae to study cellular morphology include the type 6 secretion system of *Amoebophilus asiaticus* in phagosomal escape in infected amoeba cells[50] and polyglutamine inclusions associated with Huntington's disease in the morphology of mammalian and yeast cells[51,52]. Cryo-ET of FIB-fabricated lamellae was also used to study the morphology of a phage replication compartment in infected *Pseudomonas chlororaphis* and to show how viral capsids migrate from the bacterial membrane toward this compartment via virally encoded, tubulin-like filaments[53,54].

In summary, cryo-ET on FIB-fabricated lamellae enables structural and ultrastructural studies of the cell interior in a near-native state. These studies were enabled by the development and incremental improvement of lamella fabrication, data processing and subtomogram averaging, all of which are discussed in the next section.

Recent advances in cryo-ET on FIB-fabricated lamellae

Obtaining a cellular subtomogram average structure of a macromolecule from a biological sample requires several steps, each of which must be reliable for success. For low-copy-number macromolecules, a large number of tomograms need to be acquired, underlining the importance of sample throughput. In this section, we describe the latest improvements in sample preparation (specifically vitrification and lamella fabrication), tilt-series acquisition and data processing and how to find macromolecules in the tomographic volume of the crowded cellular environment.

Sample vitrification

For cryo-ET on FIB-fabricated lamellae, cells need to be applied to or grown on an electron microscopy grid compatible with a transmission

electron microscope and FIB/SEM. Gold or titanium[55] grids are typically used because they are nontoxic to cells, stronger and less expensive. Only single cells, or small clusters of cells, that are located near the center of the grid and center of the grid squares are suitable for FIB milling, which can greatly reduce the number of sites available for lamella fabrication[15]. Photo-micropatterning can be used to make cells selectively adhere to the center of the grid squares[55].

Cells on an electron microscopy grid are then rapidly frozen to preserve the fine structural and ultrastructural features. Ideally, all cells end up in a vitreous state, which preserves them under near-native conditions without the formation of crystalline ice, which would disrupt the structure of the cell[4]. The most commonly used ultrarapid freezing technique for cellular samples is plunge freezing, which involves quickly submerging the sample into liquid ethane or a mixture of liquid ethane and propane and cooling with liquid nitrogen to cryogenic temperatures[56–58]. A limitation of plunge freezing is that it does not have a cooling rate high enough to fully vitrify samples more than a few µm thick, such as most mammalian cells[20]. The use of a cryoprotectant such as glycerol can benefit the vitrification of cells with plunge freezing[59]. Higher cooling rates have been observed with jet freezing, where a cryogen is jetted onto the center of the sample[34,60,61]. Optimization of jet freezing or other ultrarapid freezing techniques such as slam freezing[62,63] may potentially improve the vitrification of eukaryotic cells for cryo-ET.

High-pressure freezing (HPF) can vitrify thicker samples, such as multicellular organisms, tissue and organoids, by greatly increasing the pressure to 210 MPa less than 1 s before ultrarapid freezing of the sample, which inhibits expansion of the volume during crystalline ice formation, effectively lowering the cooling rate that is required to form vitreous ice[64]. However, HPF generally results in a thick layer of ice surrounding the biological sample that can be too large to remove with the FIB. Harapin et al.[65] describe how a biological sample high-pressure frozen in 2-methylpentane can be thinned by sublimation of the 2-methylpenthane in a vacuum at temperatures below the devitrification temperature of ice. However, the biological sample is exposed to an organic solvent during the freezing process and requires long milling times (>1 d) for bulkier samples with a conventional gallium FIB. HPF can be used to ultrarapidly freeze smaller cells with less ice surrounding them to allow direct lamella preparation by sandwiching the grid between two polished planchettes[66]. Another strategy involves cutting back the planchette with a cryo-ultramicrotome so that lamellae can be prepared near the cutting edge[67].

FIB fabrication of lamellae

After freezing, lamella fabrication can be performed with a FIB–SEM dual-beam microscope. The FIB is used to remove all of the material above and below part of the cell, leaving a ~200 nm layer of vitreous cellular material suitable for cryo-ET[14,15] (Fig. 1e–h). The lamella surface area depends on the cell type, the chosen lamella width and the milling angle. For mammalian cells, the width is typically between 8 and 20 µm and the length is between 5 and 40 µm. Because the commonly used gallium FIB has a Gaussian distribution[68], lamellae are often thinner at the front compared with the back. A more even lamella thickness can be achieved by slightly tilting the sample during the milling process to produce a wedge geometry, followed by a fine milling step at the original milling angle[14]. Another common problem is the occurrence of cracks in lamellae caused by a build up of tension in the grid foil. This cracking can be mitigated by creating micro-expansion joints during the first milling step to release the tension[69] (Fig. 1g,h).

Manual FIB fabrication of lamellae is a time-consuming process. An experienced user can create 5–16 lamellae per day[69,70]. Automated lamella fabrication[71–73] can run overnight and greatly increase throughput. However, the number of lamellae milled from a single grid is limited by the rate at which water vapor is deposited on the sample due to the high partial H_2O pressure conditions in the sample chamber. Cryo-FIB–SEM microscopes for lamella fabrication can have a continuous deposition of water vapor on the finished lamellae at a rate of up to 85 nm h^{-1} (refs. [14,73]). The accumulation of the ice layer, as well as deposition of sputtered material on the lamella, can be decreased by performing the final milling steps of each lamella last, but it still in practice limits the number of lamellae from a single grid to 3–5.

Bringing the sublimation and deposition rates in the FIB–SEM chamber closer to equilibrium can reduce the ice growth rate. Tacke et al.[73] accomplished this by installing additional cryo-shields and a cryo-shutter (which reduces the opening for the ion beam) in the FIB–SEM sample chamber to decrease the partial water vapor pressure and by using a heater to heat the sample to −165 °C; these modifications decreased the ice growth rate to 5.6 nm h^{-1}. The ice growth rate could be further reduced to 0–2 nm h^{-1} by employing a different cryo-shutter that further decreases the opening for the ion beam and completely blocks the electron beam. Additionally, the authors showed reduced ice contamination by using a glove box flushed with nitrogen gas for sample handling and by performing sample unloading in a vacuum during the brief transfer from the transfer rod to the liquid nitrogen in the loading station[73]. Ice growth rates of <2 nm have also been reported recently[35].

Lamellae of larger samples can be created by extracting biological material with a FIB lift-out approach. With this method, a 3- to 5-µm-thick lamella is created perpendicular to the surface of a high-pressure frozen sample and transferred to a slot on another grid with a cryo-micromanipulator[74–77] or cryo-gripper[78,79], followed by fine FIB fabrication of lamellae. The thick ice layer can be removed with a cryo-microtome or freeze fracturing before the lift-out procedure[80,81]. Since high-pressure-frozen samples are generally surrounded by ice, the biological specimen cannot always be found with FIB or SEM imaging, resulting in a substantial risk of missing the cells entirely. CLEM can be used to determine where fluorescently labeled cells are located in the ice[71,75,78].

While gallium ion beams are most commonly used for cryo-FIB fabrication of lamellae, a plasma FIB using other elements (for example, xenon, argon, nitrogen or oxygen) may speed up lamellae fabrication and bulk removal for lift-out approaches[78]. Xenon plasma FIBs are reported to have faster milling rates compared with gallium, with a decreased depth of the damage layer in material science applications[82,83]. A recent study showed that argon is suitable for preparing FIB-fabricated lamellae for subtomogram averaging in an automated fashion, enabling a 4.9 Å structure of the 80S human ribosome in HeLa cells to be determined[35].

Cryo-ET on FIB-fabricated lamellae

After lamella fabrication, tilt series of the lamellae are acquired with a cryogenic transmission electron microscope. Cryo-ET benefits from the same technical improvements that enabled the resolution revolution in single-particle cryo-EM, in particular direct electron detectors and processing software (see the section 'Data processing for subtomogram averaging')[1,84]. A limitation of tomography is the restricted tilt range of ~120°, which results in missing information in reciprocal space in the direction of the electron beam (that is, a missing wedge). This missing wedge results in lower resolution in the direction of the electron beam and reconstruction artifacts in tomograms. Limitations of the missing wedge can be alleviated for randomly oriented macromolecular complexes (but not for those of the preferred orientation) during subtomogram averaging.

The use of an energy filter can increase the contrast in thicker samples by removing inelastic scattered electrons, which is particularly beneficial for cellular cryo-ET. A phase plate, which (ideally) shifts electrons 90° in phase to maintaining a good transfer of low-spatial-frequency information, can be used to acquire tilt series close to focus while retaining good contrast. For the most commonly used Volta phase plates, this is achieved by creating a beam-induced Volta

potential on a heated carbon film of ~12 nm in the back focal plane of the transmission electron microscope[85]. The disadvantages of Volta phase plates include the scattering of electrons from passing through the carbon film, the technical challenges of maintaining a consistent focus and phase shift due to variability in the phase shift from charging of the carbon film and the increased difficulty of accurate contrast transfer function (CTF) estimation and correction of the data[86]. A 5–20 nm platinum layer applied on lamellae after FIB milling improved the conductivity and decreased sample charging during Volta phase plate experiments[14]. Early results with laser phase plates, which use the standing light wave from a laser rather than a film to create a phase shift, indicate that they have the potential for more stable phase shifts, without electron scattering from a carbon film[87].

The transfer of high-resolution information in the tilt series can be improved by adopting a dose-symmetric tilt scheme where the lowest tilt angles are imaged first. This strategy minimizes the cumulative damage from the electron beam at the angles where the sample is effectively the thinnest because of the geometry of the lamella[86,88]. Dramatic increases in the rate of tilt-series acquisition to several minutes per tilt series have been reported with fast-incremental tilt schemes, where autofocus and tracking steps are omitted and movie frames are continuously recorded while stopping at different tilt angles to record an image by unblanking the electron beam[89,90]. The use of this tilt scheme enabled a subtomogram-averaged structure of isolated ribosomes at subnanometer resolution on a dataset of 12 tilt series recorded in 50 min[90]. This rapid acquisition time contrasts with commonly used tilt schemes requiring 20–60 min per tilt series. Another alternative faster tilt scheme uses beam shift (with correction for variable beam tilt as a function of beam shift) to acquire several images per tilt, effectively allowing tilt series to be acquired in 5 min without sacrificing data quality[91]. Montage tomography using beam shift, optimized to decrease fringe artifacts on the electron beam edges and with minimal excessive electron dose on areas exposed multiple times, is also being developed to acquire volumetric data over a larger area on FIB-fabricated lamellae[92].

Data processing for subtomogram averaging

Data processing aims to correct some of the aberrations caused by the electron microscope during imaging to improve the resolution of the data and the resulting structures. Irradiation by the electron beam introduces motions to the sample during the acquisition. A series of images acquired at a single tilt angle with a direct electron detector can correct for this beam-induced motion in a process termed motion correction[93]. Electrons also cause cumulative damage to the sample during the acquisition of a tilt series, which can be compensated for with dose weighting[94], where the more dose-sensitive, high-spatial-frequency information of fine molecular details is downweighed in tilts acquired later. Finally, image acquisition with an electron microscope results in an oscillating pattern of contrast loss and reversals as a function of spatial frequency (CTF), which is strongly affected by the defocus[8]. CTF correction is essential to achieve high resolution in a subtomogram-averaged structure. Where local variations in defocus from sample tilt are corrected for by most methods[95,96], more advanced 3D CTF correction methods can better adjust for the local defocus of a particle by taking into account its height (z) within the sample[97–101].

Tilt series also need to be accurately aligned for 3D tomogram reconstruction, since this affects the final resolution[86,99,100]. Accurate local alignments are preferred over global alignments to better correct for complex sample motions and deformation during tilt-series acquisition[101]. Tilt-series alignment is most commonly performed with patch tracking, which tracks cellular features based on cross-correlations[15,96]. However, more accurate local alignment can be achieved with fiducial-based alignment. Colloidal nanogold particles (5–20 nm) act as fiducials when mixed with small cells (such as bacteria) before ultrarapid freezing, but do not give a good distribution for larger eukaryotic cells. Endocytosis of bovine serum albumin–nanogold by mammalian cells before ultrarapid freezing can be used to distribute fiducials throughout the cell, which can be used for tilt-series alignment after lamella preparation[102]. To apply gold fiducials to lamellae after fabrication, nanogold can be resuspended in 2-methylpentane and applied to the surface of the lamellae[65].

Numerous software packages have been developed over the years to obtain structures of macromolecules from tomograms[94,99–101,103]. The recently developed software packages EMAN2, emClarity and M correct imaging artifacts locally, per particle[99–101], which improves the resolution that can be obtained with subtomogram averaging. For example, the software package M refines several per-particle parameters, including alignment and CTF correction, in an iterative process and constrains these based on other particles from the same tilt series[101]. Artifacts from intermediate interpolations are minimized by directly reconstructing the final subtomogram average map from the motion-corrected tilt series rather than extracted subtomograms. When several different local corrections are applied together, this combination results in a sizable increase in resolution[99–101]. Promising subnanometer-resolution structures have also been obtained with tomography and single-particle hybrid approaches[104,105], but their use on lamellae has not yet been reported.

Interpreting tomograms of the crowded cellular environment

While visualizing the native cellular environment is the main strength of cryo-ET on lamellae, it also makes interpretation of the crowded cellular environment challenging. Numerous different macromolecules in the cell and the typically low signal-to-noise ratio in cellular tomograms make it difficult to find specific macromolecules. Localizing macromolecules (often done by hand) is essential for subtomogram averaging. The identifiable macromolecules depend on many factors, including size, shape, the relative density compared with the surrounding medium, the local crowdedness of the tomogram and experience and biological understanding of the researcher.

A proven method for identifying the location of macromolecules in room temperature electron microscopy is the use of nanogold particles conjugated to antibodies that specifically bind to the macromolecule in a cellular section (that is, immunogold labeling). Robust labeling strategies for cryogenic applications may be of considerable benefit in localizing and identifying macromolecular complexes. It has been demonstrated that SNAP-tag-labeled nanogold[106] and immunogold labeling on live cells before freezing can label proteins on extracellular membrane surfaces[107,108]. A recent study also showed that DNA origami structures with a high affinity for green fluorescent protein (GFP) can be used to specifically label proteins on the surface of cells and viruses before sample freezing[109]. Iron-binding ferritin fusion proteins have also been shown to enable intracellular labeling of bacteria visible in cryo-EM[110]. In principle, a fluorescent label combined with high-accuracy cryo-CLEM can be used to find macromolecules of interest (discussed in the section 'CLEM').

In addition to labeling, unknown proteins in a complex have been identified in lamellae using genetic modification. For example, deletion mutants enabled the identification of FraD as a structural component of the plug of the septal gap junction protein in cyanobacteria[39]. In another study, expression of an nsp3-EGFP fusion protein[40] facilitated the discovery of nsp3 as a structural component of the pore that spans the coronavirus replication compartment.

Identifying macromolecules of interest can be facilitated by various computational methods (reviewed in ref. [111]). One such approach denoises tomograms with filters to greatly increase their visual clarity and improve the signal-to-noise ratio[96,100,112,113]. More recently, image restoration based on machine learning has shown promising results[114–116]. Computational subtraction can diminish artifacts resulting from the thin platinum layer sputtered on the finished lamellae[14], contaminants and/or nanogold fiducials[96,117].

Finding known macromolecular complexes can be automated with template matching, where the density of a known macromolecule is compared with the tomographic volume at different orientations by means of cross-correlation[103]. The chance of success depends on different factors, including the macromolecule (for example, size, shape, the distinctness of the density and the subcellular environment) and the tomographic data (for example, quality, resolution and crowdedness). Algorithms that use machine learning[118–120], pattern mining[121] and software for identifying membrane-bound and transmembrane macromolecular complexes[122] have been developed recently to assist in finding unknown macromolecules without an existing template.

Another process that can assist in interpreting the cell environment is segmentation, where cell membranes are traced in the volume, to enable quantifications of membrane curvature, surface area and distance of macromolecules to membranes. While manual segmentation is time consuming, (semi-)automated methods have been demonstrated[123,124] and successfully applied in different studies[48,49,51,54]. The quality of segmentation can be improved with post-processing, such as low-pass filtering or mean curvature motion[125].

CLEM

Cryo-EM methods can achieve atomic-resolution structures, but the low signal-to-noise ratio can make it difficult to locate macromolecules or biological structures. Likewise, both FIB and SEM imaging are limited to obtaining morphological information of the cell surface. Cryo-CLEM can complement these imaging modalities by localizing fluorescently labeled macromolecules and/or biological structures in the sample and providing contextual information about the cell interior. CLEM techniques were first developed for classical electron microscopy on chemically or cryogenically fixed, resin-embedded samples at room or low temperature followed by room temperature electron microscopy observation[126], and later adapted for use under cryogenic conditions[127,128]. This adaptation came with a unique set of challenges, in particular for super-resolution light microscopy. In this section, we first describe different applications for CLEM in the context of cryo-ET on FIB-fabricated lamellae, followed by the challenges and developments in pushing the resolution with cryogenic light microscopy (cryo-LM).

CLEM applications for cryo-ET on FIB-fabricated lamellae

One application of CLEM for FIB-fabricated lamellae is to use light microscopy to help determine which cells to use for FIB fabrication of lamellae, for which a coarse correlation accuracy (up to several micrometers) between light microscopy and SEM data is sufficient. Examples include finding the subcellular localization of actin waves[129], different disease-associated fluorescently labeled mutants of proteins[51,52], cells in a specific stage of the cell cycle[130] or cells infected with a pathogen (Fig. 3a,b).

Light microscopy data can be acquired before ultrarapid freezing[51], which allows the use of oil immersion objectives with a high numerical aperture, as well as live imaging over time[26]. The major disadvantage is that the live sample changes over time between light microscopy acquisition and sample freezing, making the correlation inaccurate for fast and dynamic processes. The time between imaging and freezing can be minimized to seconds using a plunge freezer with an integrated fluorescence microscope[131] or to milliseconds using a cryo-fixation microfluidics device that freezes the sample with a liquid nitrogen-cooled heat sink[79]. The cooling rate of this microfluidics device was sufficient to vitrify larvae of *C. elegans* in 10% glycerol, which could subsequently be imaged with cryo-ET with a FIB lift-out approach.

Light microscopy data can also be acquired post-vitrification, where all biological processes are arrested. To enable this, dedicated cryogenic stages[127,128,132–134] maintain the sample below the devitrification temperature, minimize drift, allow for fast cryogenic transfers and provide a low-humidity environment to minimize ice contamination on the sample while imaging. Integrated approaches, where light microscopy is combined in a transmission electron microscope or FIB–SEM microscope, can also minimize ice contamination by decreasing cryogenic transfer and allow cryo-LM imaging in a vacuum environment, enabling easier and faster correlations[81,135].

Since lamellae have a local thickness of 50–300 nm and cells are typically micrometer sized, only a fraction of the total cellular volume is contained in a prepared lamella. Macromolecules, cellular structures and interactions of interest that are not ubiquitously expressed throughout the cell may have a low chance of being contained within the prepared lamella. Cryo-CLEM can help pinpoint where to prepare lamellae to contain the target[30,46]. One approach uses electron-dense, micrometer-sized fluorescent fiducials visible in both the FIB–SEM and light microscopy to calculate the transformation parameters (scaling, translations and rotations) to correlate 3D light microscopy data to a 2D FIB image (Fig. 3c,d)[134]. Arnold et al.[134] reported a ≥150 nm localization accuracy on 60% of targets (polystyrene beads) with this method. The accuracy on intracellular targets may be lower because of optical distortions from refractive index mismatches between the cell and the gaseous environment[136] and sample distortions during FIB fabrication of lamellae[71]. This approach requires axial localization of fiducials and the structure of interest with an accuracy of hundreds of nanometers to achieve consistent targeting, depending on the size of the target. A recent study reported a ~91% success rate in targeting the centrosome for FIB fabrication of lamellae, by using a widefield microscope mounted underneath the sample in the FIB–SEM microscope, which can be operated during milling[135]. Targeting is achieved by first calibrating the coincidence point for the FIB, SEM and light microscopy, followed by focusing and centering of the intracellular target of interest[135,137]. Serial cryo-FIB–SEM imaging, where thin layers of cellular material are removed with the FIB, followed by SEM imaging to obtain 3D data, has also been successfully employed to help determine where the final lamella is formed[138]. More importantly, it provides morphological context of the cellular material that is otherwise removed without imaging, and can be correlated with cryo-LM to obtain specific information about the cell.

In another application, cryo-CLEM is used to identify areas of interest in the prepared lamellae, which can help to determine where to acquire tilt series or to identify macromolecules in the crowded cellular environment (Fig. 3e–h). Only a low correlation accuracy below the field of view used for tomography (typically 1–2 µm) is required for its successful application. A CLEM approach combined with split-Venus labeling was used to identify areas where nuclear core complexes interact with autophagosomes in the final lamellae to record tilt series of it[30]. Current challenges for acquiring fluorescence data after FIB fabrication of lamellae are that the fluorescent signal may be difficult to detect and that cryogenic transfers to a cryo-LM may directly contaminate the lamellae with ice[42,81]. In another approach where fluorescence light microscopy data are acquired before FIB fabrication of lamellae, a tilt-corrected optical slice is extracted that matches with the final lamella. The tilt of the lamella is determined by recording transmitted light brightfield data of the lamella after transmission electron microscopy (TEM) imaging[42]. The downside of recording fluorescence data before lamella fabrication is that the signal from out-of-focus objects that are not present in the lamella may still be present in the correlated optical slice due to the limited axial (z) resolution of light microscopy[42]. In principle, cryo-LM can be correlated to tomographic data to help pinpoint the 3D location of labeled macromolecules within tomograms. In practice, this is not yet feasible due to the limited resolution of cryogenic fluorescence microscopy.

Pushing the resolution beyond the diffraction limit in cryo-LM

Since the correlation accuracy of CLEM applications for FIB-fabricated lamellae depends greatly on the resolution of the light miscroscopy, increasing the resolution obtained under cryogenic conditions is critical. In light miscroscopy at room temperature, the diffraction-limited

https://doi.org/10.1038/s41592-023-01783-5

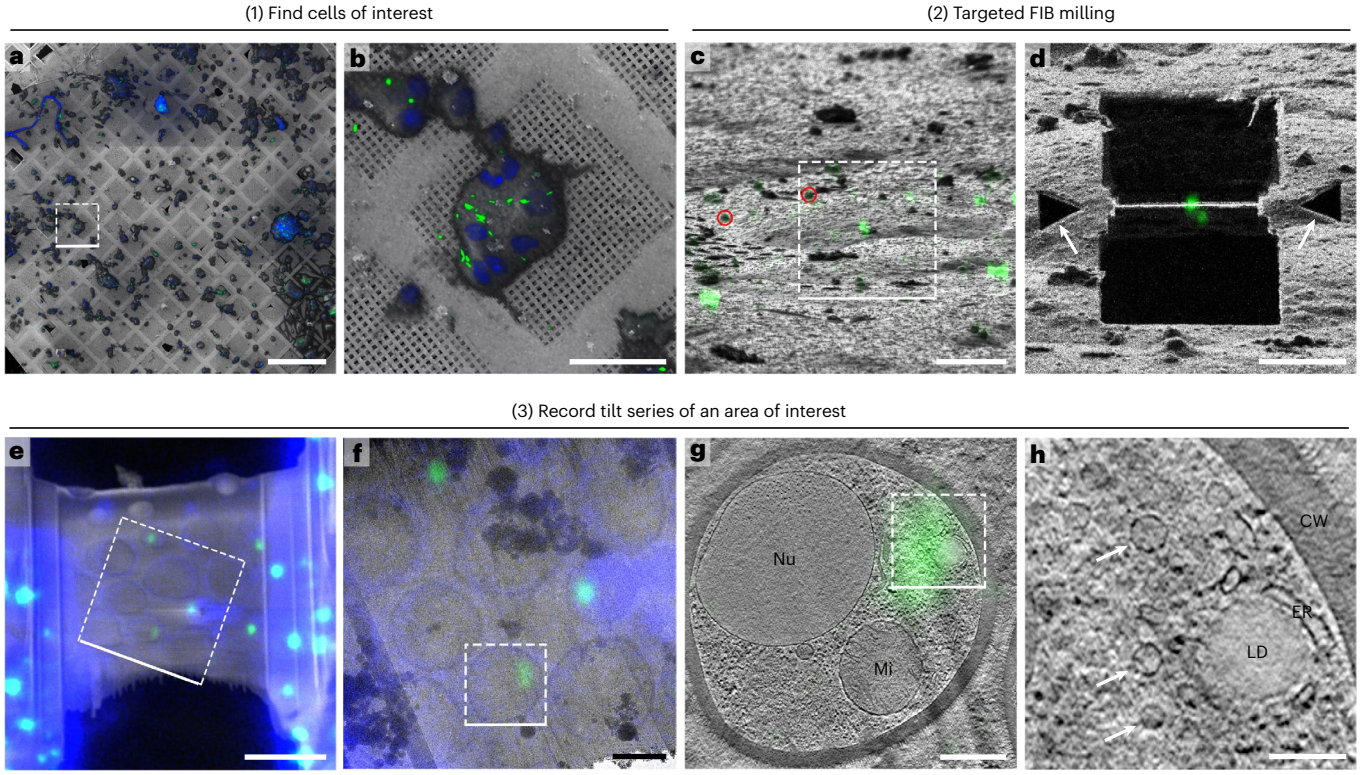

Fig. 3 | Three examples of distinct applications of CLEM for cryo-ET on FIB-fabricated lamellae. White dashed boxes indicate the sections that are magnified in the next panel, with a solid white line indicating the bottom side of the next panel. Note that the enlarged area in **f** from **e** has been rotated. **a**,**b**, 2D–2D correlation of cryo-LM with a SEM image to find cells of interest before FIB milling. Macrophages were differentiated from primary blood monocytes grown on an electron microscopy grid and infected with *Mycobacterium marinum*. The nuclei are labeled in blue and the bacteria are labeled in green. Scale bars, 300 µm (**a**) and 50 µm (**b**). **c**, Targeted FIB milling approach using CLEM to make a lamella of a cell containing a macromolecular complex or structure of interest. A cryo-LM *z* stack is correlated with a FIB image at the milling angle using fiducials visible with both the FIB and light microscopy (red circles) and projected into a 2D image. This 2D projection is overlaid with a FIB image and can be used to target the position for a FIB-fabricated lamella so that it contains a biological target of interest. In this example, macrophages were infected with *Escherichia coli* expressing a fluorescent protein. Scale bar, 10 µm. **d**, FIB image after FIB fabrication of a lamella overlaid with the projected 2D fluorescence image via the image in **c** using the software eC-CLEM[155]. Triangular markers were prepared with FIB (white arrows) on the side of the lamella at the start of fabrication to determine where the final lamella should be made in subsequent finer milling steps. The presence of fluorescence on the final lamellae suggests that the targeted fluorescent bacteria are probably contained within the lamella. This was later confirmed to be the case with cryo-EM (data not shown). Scale bar, 5 µm. **e**, 2D–2D correlation to find areas for recording tilt series containing a macromolecule, complex or structure of interest. In this example, the aim was to find preperoxisomal vesicles by overexpressing the peroxisomal membrane protein-14 (Pex14) fused to GFP (green) in yeast (*Hansenula polymorpha* Δ*PEX19*). The cell wall was labeled in blue to correlate cryo-LM to electron microscopy images. Cryo-LM was acquired after FIB fabrication of a lamella so that only fluorescence from macromolecules still present in the lamella was retained. A 2D cryo-LM image was correlated to the SEM overview of the lamella after final fabrication using the software eC-CLEM[155]. Scale bar, 5 µm. **f**, Low-dose cryo-TEM overview of the same lamella (enlarged from the boxed area in **e**) correlated to the cryo-LM image to determine where to record the tilt series. Scale bar, 1 µm. **g**, Summed tomographic slices from a tilt series recorded on the lamella (enlarged from the boxed area in **f**) correlated to the green fluorescent signal to indicate where preperoxisomal vesicles should be located within the tomogram. Both the nucleus (Nu) and a mitochondrion (Mi) are clearly visible. Scale bar, 500 nm. **h**, Enlarged section of the same summed tomographic slices (dashed box in **g**) where several preperoxisomal vesicles are visible (white arrows). A lipid droplet (LD) is surrounded by the endoplasmic reticulum and the cell is surrounded by the cell wall (CW). Scale bar, 100 nm.

lateral resolution is normally 200–300 nm, which is largely dependent on the wavelength of the emitted fluorescence and the numerical aperture of the objective. The resolution obtained for cryo-LM is typically lower due to several challenges at cryogenic conditions.

One limitation is the difficulty of developing immersion objectives for cryogenic conditions with a high numerical aperture, which limits the photon yield and resolution. Where oil immersion objectives with a numerical aperture of ~1.4 can be employed at room temperature, only air objectives, for which the numerical aperture is fundamentally limited to below 1, can be used for cryo-LM. Several approaches have been explored to overcome this, such as the use of an immersion objective together with cryogenic immersion fluids with a matching refractive index[139,140] or an air objective together with a superhemispherical solid immersion lens to bridge the distance between the objective and the sample[141].

Imaging beyond the diffraction limit at room temperature was enabled by the development of several super-resolution techniques[142–144], many of which have been successfully demonstrated at cryogenic temperatures. Although these super-resolution techniques have not yet been reported for cryo-ET on FIB-fabricated lamellae, they can benefit accurate CLEM (reviewed in ref. [136]). The application of super-resolution light microscopy in CLEM approaches for FIB-fabricated lamellae can provide a substantial increase in resolution and localization precision and help to reduce the current resolution gap with cryo-EM. Considerable progress has been made in the development of localization-based super-resolution cryo-LM[139,141,145] and used to study biological samples, including the type 6 secretion system in *Myxococcus xanthus* and *Vibrio cholerae*[146], localization of TOM20 in cryogenic sections of mammalian cells[147] and several bacterial proteins in *Caulobacter crescentus*[148]. A recent study showed successful cryo-CLEM on tomograms recorded

on the mammalian cell periphery with a localization precision of 30 nm[149]. One challenge for localization-based super-resolution cryo-LM is that fluorophores have altered photoswitching behavior compared with at room temperature, which requires the use of high laser powers to make them adopt a dark state[139,140,145–147,149] and thus may devitrify the sample[146,147,149]. One study reported that photoswitchable fluorescent proteins can be forced into their deactivated state and retained for at least 7 d after freezing by illuminating the sample before ultrarapid freezing[149]. Super-resolution optical fluctuation imaging, which pinpoints fluorophores based on bulk fluorescence intensity fluctuations rather than isolated blinking events, has been applied to lower the laser power as well as acquisition times. Super-resolution optical fluctuation imaging has been successfully demonstrated under cryogenic conditions to visualize conventional cryo-EM samples without cryoprotectant, with a resolution up to 135 nm[150]. The nonlocalization-based super-resolution techniques structured illumination microscopy and Airyscan confocal microscopy have also been successfully applied under cryogenic conditions, resulting in lateral resolutions of up to 200 and 290 nm, respectively, using air objectives[151,152].

The future of cellular cryo-ET

While cryo-ET on FIB-fabricated lamellae has developed into a powerful technique over the past few years to elucidate the profound structural complexity of the cell, its full potential has not yet been achieved. The resolutions obtained with subtomogram averaging are steadily improving[35,36,38,101] and subnanometer or even near-atomic resolution in situ structures for many macromolecules can be attained using cryo-ET on FIB-fabricated lamellae. One of its current limitations is low throughput due to the limited speed and success rate of each individual step.

First, sample preparation of thick cells, organoids, multicellular organisms and tissues requires further improvement. Incomplete vitrification of large cells with plunge freezing limits the throughput and cell types that can be effectively studied. Adaptation of HPF sample holders[66] or the development of other ultrarapid freezing techniques[61,62,79] compatible with subsequent cryo-ET provides hope for improved vitrification of more (and larger) cell types. While impressive results have been obtained with FIB lift-out approaches on multicellular organisms, the current success rate of ~20% is too low for most in situ structural studies[78].

To increase throughput, the rate of FIB fabrication of lamellae could be increased with an automated FIB–SEM dual-beam microscope[71,73] with minimal ice growth and contamination from transfer[73]. Faster tilt-series acquisition schemes[89–91] can substantially speed up tomography data acquisition.

Further automation of data processing, tomogram reconstruction, data analysis and subtomogram averaging, which are arguably larger bottlenecks than data acquisition, would also improve throughput. The application of machine learning for image restoration and denoising[114–116], map denoising[101], locating macromolecules in tomograms[119–122] and automated reconstruction[153] could help improve the speed and accuracy of the different processing steps. The rapid improvements for machine learning applications, such as the recent success of AlphaFold 2 (ref. [154]) in predicting protein structures, will also facilitate these advancements.

With increased throughput and structures of increased resolution and from a greater range of macromolecules, new types of research will become feasible. For example, in situ structure determination of smaller macromolecules and the detection of more subtle conformational states may be possible. Hundreds or even thousands of different macromolecules (both known and unknown) in different conformational states could be identified in tomographic volumes and linked to their subcellular localization, bringing visual proteomics closer to becoming a reality[43]. This in situ structural information could be established over a wide range of species and cell types, for different diseases and under different physiological conditions and stimuli. Effective sharing and open access to annotated cellular tomographic data could accelerate such an endeavor[101].

In summary, developments in cryo-ET and FIB fabrication of lamellae over the past years have demonstrated remarkable advancements, enabling in situ structural studies that were not previously possible. Major challenges are still present, but resolving the current shortcomings can greatly expand what is possible in in situ structural biology and advance our understanding of macromolecular structures in relation to their function and subcellular localization—effectively bridging the gap between structural and cell biology. Cryo-ET on FIB-fabricated lamellae, and its contributions to in situ structural biology, may soon prove to be the second wave in the cryo-EM revolution.

References

1. Kuhlbrandt, W. The resolution revolution. *Science* **343**, 1443–1444 (2014).
2. Nakane, T. et al. Single-particle cryo-EM at atomic resolution. *Nature* **587**, 152–156 (2020).
3. Yip, K. M., Fischer, N., Paknia, E., Chari, A. & Stark, H. Atomic-resolution protein structure determination by cryo-EM. *Nature* **587**, 157–161 (2020).
4. Dubochet, J. et al. Cryo-electron microscopy of vitrified specimens. *Q. Rev. Biophys.* **21**, 129–228 (1988).
5. Medalia, O. Macromolecular architecture in eukaryotic cells visualized by cryoelectron tomography. *Science* **298**, 1209–1213 (2002).
6. Dobro, M. J. et al. Uncharacterized bacterial structures revealed by electron cryotomography. *J. Bacteriol.* **199**, 1–14 (2017).
7. Walz, J. et al. Tricorn protease exists as an icosahedral supermolecule in vivo. *Mol. Cell* **1**, 59–65 (1997).
8. Wan, W. & Briggs, J. A. G. Cryo-electron tomography and subtomogram averaging. *Methods Enzymol.* **579**, 329–367 (2016).
9. McDowall, A. W. et al. Electron microscopy of frozen hydrated sections of vitreous ice and vitrified biological samples. *J. Microsc.* **131**, 1–9 (1983).
10. Al-Amoudi, A., Norlen, L. P. O. & Dubochet, J. Cryo-electron microscopy of vitreous sections of native biological cells and tissues. *J. Struct. Biol.* **148**, 131–135 (2004).
11. Pierson, J., Ziese, U., Sani, M. & Peters, P. J. Exploring vitreous cryo-section-induced compression at the macromolecular level using electron cryo-tomography; 80S yeast ribosomes appear unaffected. *J. Struct. Biol.* **173**, 345–349 (2011).
12. Marko, M., Hsieh, C., Schalek, R., Frank, J. & Mannella, C. Focused-ion-beam thinning of frozen-hydrated biological specimens for cryo-electron microscopy. *Nat. Methods* **4**, 215–217 (2007).
Key study in the development of cryo-FIB lamellae preparation on biological samples.
13. Rigort, A. et al. Focused ion beam micromachining of eukaryotic cells for cryoelectron tomography. *Proc. Natl Acad. Sci. USA* **109**, 4449–4454 (2012).
14. Schaffer, M. et al. Optimized cryo-focused ion beam sample preparation aimed at in situ structural studies of membrane proteins. *J. Struct. Biol.* **197**, 73–82 (2017).
15. Wagner, F. R. et al. Preparing samples from whole cells using focused-ion-beam milling for cryo-electron tomography. *Nat. Protoc.* **15**, 2041–2070 (2020).
16. Marko, M. et al. Focused ion beam (FIB) preparation methods for 3-D biological cryo-TEM. *Microsc. Microanal.* **12**, 98–99 (2006).
17. Basgall, E. & Nicastro, D. Cryo-focused ion beam preparation of biological materials for retrieval and examination by cryo-TEM. *Microsc. Microanal.* **12**, 1132–1133 (2006).
18. Hayles, M. F., Stokes, D. J., Phifer, D. & Findlay, K. C. A technique for improved focused ion beam milling of cryo-prepared life science specimens. *J. Microsc.* **226**, 263–269 (2007).

19. Marko, M., Hsieh, C., Moberlychan, W., Mannella, C. A. & Frank, J. Focused ion beam milling of vitreous water: prospects for an alternative to cryo-ultramicrotomy of frozen-hydrated biological samples. *J. Microsc.* **222**, 42–47 (2006).
20. Mahamid, J. et al. Visualizing the molecular sociology at the HeLa cell nuclear periphery. *Science* **351**, 969–972 (2016).
Early biological study demonstrating subtomogram averaging on FIB lamellae.
21. Hagen, C. et al. Structural basis of vesicle formation at the inner nuclear membrane. *Cell* **163**, 1692–1701 (2015).
22. Bykov, Y. S. et al. The structure of the COPI coat determined within the cell. *eLife* **6**, e32493 (2017).
23. Dodonova, S. O. et al. A structure of the COPI coat and the role of coat proteins in membrane vesicle assembly. *Science* **349**, 195–198 (2015).
24. Laughlin, T. G. et al. Architecture and self-assembly of the jumbo bacteriophage nuclear shell. *Nature* **608**, 429–435 (2022).
25. Pfeffer, S. et al. Dissecting the molecular organization of the translocon-associated protein complex. *Nat. Commun.* **8**, 14516 (2017).
26. Li, X. et al. A mammalian system for high-resolution imaging of intact cells by cryo-electron tomography. *Prog. Biophys. Mol. Biol.* **160**, 87–96 (2021).
27. Kovtun, O. et al. Structure of the membrane-assembled retromer coat determined by cryo-electron tomography. *Nature* **561**, 561–564 (2018).
28. Mosalaganti, S. et al. AI-based structure prediction empowers integrative structural analysis of human nuclear pores. *Science* **376**, eabm9506 (2022).
29. Mosalaganti, S. et al. In situ architecture of the algal nuclear pore complex. *Nat. Commun.* **9**, 2361 (2018).
30. Allegretti, M. et al. In-cell architecture of the nuclear pore and snapshots of its turnover. *Nature* **586**, 796–800 (2020).
31. Zhao, Y. et al. 3D structure and in situ arrangements of CatSper channel in the sperm flagellum. *Nat. Commun.* **13**, 3439 (2022).
32. Klena, N. et al. Architecture of the centriole cartwheel-containing region revealed by cryo-electron tomography. *EMBO J.* **39**, e106246 (2020).
33. Klein, S. et al. SARS-CoV-2 structure and replication characterized by in situ cryo-electron tomography. *Nat. Commun.* **11**, 5885 (2020).
34. Berger, C. et al. Structure of the *Yersinia* injectisome in intracellular host cell phagosomes revealed by cryo FIB electron tomography. *J. Struct. Biol.* **213**, 107701 (2021).
35. Berger, C. et al. Plasma FIB milling for the determination of structures in situ. *Nat. Commun.* **14**, 629 (2023).
36. Sutton, G. et al. Assembly intermediates of orthoreovirus captured in the cell. *Nat. Commun.* **11**, 4445 (2020).
37. Wang, Z. et al. The molecular basis for sarcomere organization in vertebrate skeletal muscle. *Cell* **184**, 2135–2150.e13 (2021).
38. Wang, Z. et al. Structures from intact myofibrils reveal mechanism of thin filament regulation through nebulin. *Science* **375**, 1612–1627 (2022).
High-resolution in situ structures obtained on FIB lamellae, showing structural differences with structures obtained on isolated proteins.
39. Weiss, G. L., Kieninger, A.-K., Maldener, I., Forchhammer, K. & Pilhofer, M. Structure and function of a bacterial gap junction analog. *Cell* **178**, 374–384.e15 (2019).
40. Wolff, G. et al. A molecular pore spans the double membrane of the coronavirus replication organelle. *Science* **369**, 1395–1398 (2020).
Timely study on the structural characterisation of a molecular pore formed by coronaviruses, which were not previously structurally characterized.
41. Zhu, H. et al. In situ structure of intestinal apical surface reveals nanobristles on microvilli. *Proc. Natl Acad. Sci. USA* **119**, e2122249119 (2022).
42. Klein, S. et al. Post-correlation on-lamella cryo-CLEM reveals the membrane architecture of lamellar bodies. *Commun. Biol.* **4**, 137 (2021).
43. Nickell, S., Kofler, C., Leis, A. P. & Baumeister, W. A visual approach to proteomics. *Nat. Rev. Mol. Cell Biol.* **7**, 225–230 (2006).
44. Albert, S. et al. Proteasomes tether to two distinct sites at the nuclear pore complex. *Proc. Natl Acad. Sci. USA* **114**, 13726–13731 (2017).
45. Albert, S. et al. Direct visualization of degradation microcompartments at the ER membrane. *Proc. Natl Acad. Sci. USA* **117**, 1069–1080 (2020).
46. Guo, Q. et al. In situ structure of neuronal *C9ORF72* poly-GA aggregates reveals proteasome recruitment. *Cell* **172**, 696–705 (2018).
47. Hoffman, D. P. et al. Correlative three-dimensional super-resolution and block-face electron microscopy of whole vitreously frozen cells. *Science* **367**, eaaz5357 (2020).
48. Collado, J. et al. Tricalbin-mediated contact sites control ER curvature to maintain plasma membrane integrity. *Dev. Cell* **51**, 476–487 (2019).
49. Khanna, K. et al. The molecular architecture of engulfment during *Bacillus subtilis* sporulation. *eLife* **8**, e45257 (2019).
50. Böck, D. et al. In situ architecture, function, and evolution of a contractile injection system. *Science* **717**, 713–717 (2017).
51. Bäuerlein, F. J. B. et al. In situ architecture and cellular interactions of PolyQ inclusions. *Cell* **171**, 179–187.e10 (2017).
52. Gruber, A. et al. Molecular and structural architecture of polyQ aggregates in yeast. *Proc. Natl Acad. Sci. USA* **115**, 201717978 (2018).
53. Chaikeeratisak, V. et al. Assembly of a nucleus-like structure during viral replication in bacteria. *Science* **355**, 194–197 (2017).
54. Chaikeeratisak, V. et al. Viral capsid trafficking along treadmilling tubulin filaments in bacteria. *Cell* **177**, 1771–1780.e12 (2019).
55. Toro-Nahuelpan, M. et al. Tailoring cryo-electron microscopy grids by photo-micropatterning for in-cell structural studies. *Nat. Methods* **17**, 50–54 (2020).
56. Adrian, M., Dubochet, J., Lepault, J. & McDowall, A. W. Cryo-electron microscopy of viruses. *Nature* **308**, 32–36 (1984).
57. Frederik, P. M. & Hubert, D. H. W. Cryoelectron microscopy of liposomes. *Methods Enzymol.* **391**, 431–448 (2005).
58. Iancu, C. V. et al. Electron cryotomography sample preparation using the Vitrobot. *Nat. Protoc.* **1**, 2813–2819 (2006).
59. Bäuerlein, F. J. B., Pastor-Pareja, J. C. & Fernández-Busnadiego, R. Cryo-electron tomography of native Drosophila tissues vitrified by plunge freezing. Preprint at *bioRxiv* https://doi.org/10.1101/2021.04.14.437159 (2021).
60. Burstein, N. L., & Maurice, D. M. Cryofixation of tissue surfaces by a propane jet for electron microscopy. *Micron* **9**, 191–198 (1978).
61. Ravelli, R. B. G. et al. Cryo-EM structures from sub-nl volumes using pin-printing and jet vitrification. *Nat. Commun.* **11**, 2563 (2020).
62. Escaig, J. New instruments which facilitate rapid freezing at 83K and 6K. *J. Microsc.* **126**, 221–229 (1982).
63. Porta, D. & López-Iglesias, C. A comparison of cryo- versus chemical fixation in the soil green algae *Jaagiella*. *Tissue Cell* **30**, 368–376 (1998).
64. Moor, H., Bellin, G., Sandri, C. & Akert, K. The influence of high pressure freezing on mammalian nerve tissue. *Cell Tissue Res.* **209**, 201–216 (1980).
65. Harapin, J. et al. Structural analysis of multicellular organisms with cryo-electron tomography. *Nat. Methods* **12**, 634–636 (2015).

66. Kelley, K. et al. Waffle method: a general and flexible approach for improving throughput in FIB-milling. *Nat. Commun.* **13**, 1857 (2022).
67. Zhang, J. et al. VHUT-cryo-FIB, a method to fabricate frozen hydrated lamellae from tissue specimens for in situ cryo-electron tomography. *J. Struct. Biol.* **213**, 107763 (2021).
68. Shorubalko, I., Choi, K., Stiefel, M. & Park, H. G. Ion beam profiling from the interaction with a freestanding 2D layer. *Beilstein J. Nanotechnol.* **8**, 682–687 (2017).
69. Wolff, G. et al. Mind the gap: micro-expansion joints drastically decrease the bending of FIB-milled cryo-lamellae. *J. Struct. Biol.* **208**, 107389 (2019).
70. Medeiros, J. M. et al. Robust workflow and instrumentation for cryo-focused ion beam milling of samples for electron cryotomography. *Ultramicroscopy* **190**, 1–11 (2018).
71. Klumpe, S. et al. A modular platform for automated cryo-FIB workflows. *eLife* **10**, e70506 (2021).
72. Gorelick, S., Dierickx, D., Buckley, G., Whisstock, J. & Marco, A. Assembly and imaging set up of PIE-Scope. *Bio Protoc.* **10**, e3768 (2020).
73. Tacke, S. et al. A streamlined workflow for automated cryo focused ion beam milling. *J. Struct. Biol.* **213**, 107743 (2021).
An implementation of automated lamella fabrication, and important improvements on the FIB/SEM microscope to minimize ice growth on lamellae.
74. Rubino, S. et al. A site-specific focused-ion-beam lift-out method for cryo transmission electron microscopy. *J. Struct. Biol.* **180**, 572–576 (2012).
75. Mahamid, J. et al. A focused ion beam milling and lift-out approach for site-specific preparation of frozen-hydrated lamellas from multicellular organisms. *J. Struct. Biol.* **192**, 262–269 (2015).
76. Parmenter, C. D. & Nizamudeen, Z. A. Cryo-FIB-lift-out: practically impossible to practical reality. *J. Microsc.* **281**, 157–174 (2021).
77. De Winter, D. A. M., Hsieh, C., Marko, M. & Hayles, M. F. Cryo-FIB preparation of whole cells and tissue for cryo-TEM: use of high-pressure frozen specimens in tubes and planchets. *J. Microsc.* **281**, 125–137 (2021).
78. Schaffer, M. et al. A cryo-FIB lift-out technique enables molecular-resolution cryo-ET within native *Caenorhabditis elegans* tissue. *Nat. Methods* **16**, 757–762 (2019).
Demonstration of the lift-out technique on small organisms using a cryo-gripper, resulting in lamellae with sufficient quality for subtomogram averaging of ribosomes.
79. Fuest, M. et al. In situ microfluidic cryofixation for cryo focused ion beam milling and cryo electron tomography. *Sci. Rep.* **9**, 19133 (2019).
80. Rigort, A. et al. Micromachining tools and correlative approaches for cellular cryo-electron tomography. *J. Struct. Biol.* **172**, 169–179 (2010).
81. Gorelick, S. et al. PIE-scope, integrated cryo-correlative light and FIB/SEM microscopy. *eLife* **8**, e45919 (2019).
Integration of a fluorescence microscope in a cryo-FIB/SEM microscope for CLEM.
82. Burnett, T. L. et al. Large volume serial section tomography by Xe plasma FIB dual beam microscopy. *Ultramicroscopy* **161**, 119–129 (2016).
83. Liu, J. et al. Effect of ion irradiation introduced by focused ion-beam milling on the mechanical behaviour of sub-micron-sized samples. *Sci. Rep.* **10**, 10324 (2020).
84. Grigorieff, N. Direct detection pays off for electron cryo-microscopy. *eLife* **2**, 2–4 (2013).
85. Danev, R., Buijsse, B., Khoshouei, M., Plitzko, J. M. & Baumeister, W. Volta potential phase plate for in-focus phase contrast transmission electron microscopy. *Proc. Natl Acad. Sci. USA* **111**, 15635–15640 (2014).
86. Turoňová, B. et al. Benchmarking tomographic acquisition schemes for high-resolution structural biology. *Nat. Commun.* **11**, 876 (2020).
87. Schwartz, O. et al. Laser phase plate for transmission electron microscopy. *Nat. Methods* **16**, 1016–1020 (2019).
88. Hagen, W. J. H., Wan, W. & Briggs, J. A. G. Implementation of a cryo-electron tomography tilt-scheme optimized for high resolution subtomogram averaging. *J. Struct. Biol.* **197**, 191–198 (2017).
Implementation of a dose-symmetric tilt scheme, which has rapidly become the standard for cryo-electron tomography.
89. Chreifi, G., Chen, S., Metskas, L. A., Kaplan, M. & Jensen, G. J. Rapid tilt-series acquisition for electron cryotomography. *J. Struct. Biol.* **205**, 163–169 (2019).
90. Eisenstein, F., Danev, R. & Pilhofer, M. Improved applicability and robustness of fast cryo-electron tomography data acquisition. *J. Struct. Biol.* **208**, 107–114 (2019).
91. Eisenstein, F. et al. Parallel cryo electron tomography on in situ lamellae. *Nat. Methods* **20**, 131–138 (2023).
92. Yang, J. E. et al. Correlative cryogenic montage electron tomography for comprehensive in-situ whole-cell structural studies. Preprint at *bioRxiv* https://doi.org/10.1101/2021.12.31.474669 (2022).
93. Zheng, S. Q. et al. MotionCor2: anisotropic correction of beam-induced motion for improved cryo-electron microscopy. *Nat. Methods* **14**, 331–332 (2017).
94. Bharat, T. A. M. & Scheres, S. H. W. Resolving macromolecular structures from electron cryo-tomography data using subtomogram averaging in RELION. *Nat. Protoc.* **11**, 2054–2065 (2016).
Reliable software for cryo-EM data processing, which has increasingly become more suitable for subtomogram averaging.
95. Fernández, J. J., Li, S. & Crowther, R. A. CTF determination and correction in electron cryotomography. *Ultramicroscopy* **106**, 587–596 (2006).
96. Mastronarde, D. N. & Held, S. R. Automated tilt series alignment and tomographic reconstruction in IMOD. *J. Struct. Biol.* **197**, 102–113 (2017).
IMOD has been an invaluable tool for tomogram reconstructions and visualization for many years.
97. Turoňová, B., Schur, F. K. M., Wan, W. & Briggs, J. A. G. Efficient 3D-CTF correction for cryo-electron tomography using NovaCTF improves subtomogram averaging resolution to 3.4Å. *J. Struct. Biol.* **199**, 187–195 (2017).
98. Kunz, M. & Frangakis, A. S. Three-dimensional CTF correction improves the resolution of electron tomograms. *J. Struct. Biol.* **197**, 114–122 (2017).
99. Himes, B. A. & Zhang, P. emClarity: software for high-resolution cryo-electron tomography and subtomogram averaging. *Nat. Methods* **15**, 955–961 (2018).
100. Chen, M. et al. A complete data processing workflow for cryo-ET and subtomogram averaging. *Nat. Methods* **16**, 1161–1168 (2019).
101. Tegunov, D., Xue, L., Dienemann, C., Cramer, P. & Mahamid, J. Multi-particle cryo-EM refinement with M visualizes ribosome-antibiotic complex at 3.5Å in cells. *Nat. Methods* **18**, 186–193 (2021).
Subtomogram averaging with Warp, RELION and M allowed for pseudo-atomic structures of ribosomes to be obtained in vivo.
102. Berger, C., Ravelli, R. B. G., López-Iglesias, C. & Peters, P. J. Endocytosed nanogold fiducials for improved in-situ cryo-electron tomography tilt-series alignment. *J. Struct. Biol.* **213**, 107698 (2021).
103. Castaño-Díez, D. The Dynamo package for tomography and subtomogram averaging: components for MATLAB, GPU

computing and EC2 Amazon Web Services. *Acta Crystallogr. D Struct. Biol.* **73**, 478–487 (2017).
104. Song, K. et al. In situ structure determination at nanometer resolution using TYGRESS. *Nat. Methods* **17**, 201–208 (2020).
105. Sanchez, R. M., Zhang, Y., Chen, W., Dietrich, L. & Kudryashev, M. Subnanometer-resolution structure determination in situ by hybrid subtomogram averaging—single particle cryo-EM. *Nat. Commun.* **11**, 3709 (2020).
106. Song, K. et al. In situ localization of N and C termini of subunits of the flagellar nexin–dynein regulatory complex (N–DRC) using SNAP tag and cryo-electron tomography. *J. Biol. Chem.* **290**, 5341–5353 (2015).
107. Yi, H. et al. Native immunogold labeling of cell surface proteins and viral glycoproteins for cryo-electron microscopy and cryo-electron tomography applications. *J. Histochem. Cytochem.* **63**, 780–792 (2015).
108. Spehner, D. et al. Cryo-FIB–SEM as a promising tool for localizing proteins in 3D. *J. Struct. Biol.* **211**, 107528 (2020).
109. Silvester, E. et al. DNA origami signposts for identifying proteins on cell membranes by electron cryotomography. *Cell* **184**, 1110–1121.e16 (2021).
110. Wang, Q., Mercogliano, C. P. & Löwe, J. A ferritin-based label for cellular electron cryotomography. *Structure* **19**, 147–154 (2011).
111. Frangakis, A. S. It's noisy out there! A review of denoising techniques in cryo-electron tomography. *J. Struct. Biol.* **213**, 107804 (2021).
112. Frangakis, A. S. & Hegerl, R. Noise reduction in electron tomographic reconstructions using nonlinear anisotropic diffusion. *J. Struct. Biol.* **135**, 239–250 (2001).
113. Croxford, M. et al. Entropy-regularized deconvolution of cellular cryotransmission electron tomograms. *Proc. Natl Acad. Sci. USA* **118**, e2108738118 (2021).
114. Bepler, T., Kelley, K., Noble, A. J. & Berger, B. Topaz-denoise: general deep denoising models for cryoEM and cryoET. *Nat. Commun.* **11**, 5208 (2020).
115. Buchholz, T.-O. et al. Content-aware image restoration for electron microscopy. *Methods Cell Biol.* **152**, 277–289 (2019).
116. Tegunov, D. & Cramer, P. Real-time cryo-electron microscopy data preprocessing with Warp. *Nat. Methods* **16**, 1146–1152 (2019).
117. Fernandez, J.-J. et al. Removing contamination-induced reconstruction artifacts from cryo-electron tomograms. *Biophys. J.* **110**, 850–859 (2016).
118. Wagner, T. et al. SPHIRE-crYOLO is a fast and accurate fully automated particle picker for cryo-EM. *Commun. Biol.* **2**, 218 (2019).
119. Chen, M. et al. Convolutional neural networks for automated annotation of cellular cryo-electron tomograms. *Nat. Methods* **14**, 983–985 (2017).
120. Moebel, E. et al. Deep learning improves macromolecule identification in 3D cellular cryo-electron tomograms. *Nat. Methods* **18**, 1386–1394 (2021).
121. Xu, M. et al. De novo structural pattern mining in cellular electron cryotomograms. *Structure* **27**, 679–691.e14 (2019).
122. Martinez-Sanchez, A. et al. Template-free detection and classification of membrane-bound complexes in cryo-electron tomograms. *Nat. Methods* **17**, 209–216 (2020).
123. Martinez-Sanchez, A., Garcia, I., Asano, S., Lucic, V. & Fernandez, J. J. Robust membrane detection based on tensor voting for electron tomography. *J. Struct. Biol.* **186**, 49–61 (2014).
124. Salfer, M., Collado, J. F., Baumeister, W., Fernández-Busnadiego, R. & Martínez-Sánchez, A. Reliable estimation of membrane curvature for cryo-electron tomography. *PLoS Comput. Biol.* **16**, e1007962 (2020).
125. Frangakis, A. S. Mean curvature motion facilitates the segmentation and surface visualization of electron tomograms. *J. Struct. Biol.* **214**, 107833 (2022).
126. Deerinck, T. J. et al. Fluorescence photooxidation with eosin: a method for high resolution immunolocalization and in situ hybridization detection for light and electron microscopy. *J. Cell Biol.* **126**, 901–910 (1994).
127. Schwartz, C. L., Sarbash, V. I., Atallakhanov, F. I., Mcintosh, J. R. & Nicastro, D. Cryo-fluorescence microscopy facilitates correlations between light and cryo-electron microscopy and reduces the rate of photobleaching. *J. Microsc.* **227**, 98–109 (2007).
128. Sartori, A. et al. Correlative microscopy: bridging the gap between fluorescence light microscopy and cryo-electron tomography. *J. Struct. Biol.* **160**, 135–145 (2007).
129. Jasnin, M. et al. The architecture of traveling actin waves revealed by cryo-electron tomography. *Structure* **27**, 1211–1223.e5 (2019).
130. Chakraborty, S., Mahamid, J. & Baumeister, W. Cryoelectron tomography reveals nanoscale organization of the cytoskeleton and its relation to microtubule curvature inside cells. *Structure* **28**, 991–1003.e4 (2020).
131. Koning, R. I. et al. MAVIS: an integrated system for live microscopy and vitrification. *Ultramicroscopy* **143**, 67–76 (2014).
132. Van Driel, L. F., Valentijn, J. A., Valentijn, K. M., Koning, R. I. & Koster, A. J. Tools for correlative cryo-fluorescence microscopy and cryo-electron tomography applied to whole mitochondria in human endothelial cells. *Eur. J. Cell Biol.* **88**, 669–684 (2009).
133. Schorb, M. & Briggs, J. A. G. Correlated cryo-fluorescence and cryo-electron microscopy with high spatial precision and improved sensitivity. *Ultramicroscopy* **143**, 24–32 (2014).
134. Arnold, J. et al. Site-specific cryo-focused ion beam sample preparation guided by 3D correlative microscopy. *Biophys. J.* **110**, 860–869 (2016).
135. Li, S. et al. ELI trifocal microscope: a precise system to prepare target cryo-lamellae for in situ cryo-ET study. *Nat. Methods* https://doi.org/10.1038/s41592-022-01748-0 (2023).
136. Derosier, D. J. Where in the cell is my protein?. *Q. Rev. Biophys.* **54**, e9 (2021).
137. Boltje, D. B. et al. A cryogenic, coincident fluorescence, electron and ion beam microscope. *eLife* **11**, e82891 (2022).
138. Wu, G.-H. et al. Multi-scale 3D cryo-correlative microscopy for vitrified cells. *Structure* **28**, 1231–1237.e3 (2020).
139. Nahmani, M., Lanahan, C., DeRosier, D. & Turrigiano, G. G. High-numerical-aperture cryogenic light microscopy for increased precision of superresolution reconstructions. *Proc. Natl Acad. Sci. USA* **114**, 3832–3836 (2017).
140. Faoro, R. et al. Aberration-corrected cryoimmersion light microscopy. *Proc. Natl Acad. Sci. USA* **115**, 1204–1209 (2018).
141. Wang, L. et al. Solid immersion microscopy images cells under cryogenic conditions with 12 nm resolution. *Commun. Biol.* **2**, 74 (2019).
142. Betzig, E. et al. Imaging intracellular fluorescent proteins at nanometer resolution. *Science* **313**, 1642–1645 (2006).
143. Klar, T. A., Jakobs, S., Dyba, M., Egner, A. & Hell, S. W. Fluorescence microscopy with diffraction resolution barrier broken by stimulated emission. *Proc. Natl Acad. Sci. USA* **97**, 8206–8210 (2000).
144. Dickson, R. M., Cubitt, A. B., Tsien, R. Y. & Moerner, W. E. On/off blinking and switching behaviour of single molecules of green fluorescent protein. *Nature* **388**, 355–358 (1997).
145. Kaufmann, R. et al. Super-resolution microscopy using standard fluorescent proteins in intact cells under cryo-conditions. *Nano Lett.* **14**, 4171–4175 (2014).
146. Chang, Y.-W. et al. Correlated cryogenic photoactivated localization microscopy and cryo-electron tomography. *Nat. Methods* **11**, 737–739 (2014).

147. Liu, B. et al. Three-dimensional super-resolution protein localization correlated with vitrified cellular context. *Sci. Rep.* **5**, 13017 (2015).
148. Dahlberg, P. D. et al. Cryogenic single-molecule fluorescence annotations for electron tomography reveal in situ organization of key proteins in *Caulobacter*. *Proc. Natl Acad. Sci. USA* **117**, 202001849 (2020).
149. Tuijtel, M. W., Koster, A. J., Jakobs, S., Faas, F. G. A. & Sharp, T. H. Correlative cryo super-resolution light and electron microscopy on mammalian cells using fluorescent proteins. *Sci. Rep.* **9**, 1369 (2019).
Study demonstrating localization-based super-resolution cryo-fluorescence microscopy on mammalian cells and characterization of the light intensities that can be used without devitrifying samples.
150. Moser, F. et al. Cryo-SOFI enabling low-dose super-resolution correlative light and electron cryo-microscopy. *Proc. Natl Acad. Sci. USA* **116**, 4804–4809 (2019).
151. Phillips, M. A. et al. CryoSIM: super-resolution 3D structured illumination cryogenic fluorescence microscopy for correlated ultrastructural imaging. *Optica* **7**, 802–812 (2020).
152. Sexton, D. L., Burgold, S., Schertel, A. & Tocheva, E. I. Super-resolution confocal cryo-CLEM with cryo-FIB milling for in situ imaging of *Deinococcus radiodurans*. *Curr. Res. Struct. Biol.* **4**, 1–9 (2022).
153. Gupta, H., McCann, M. T., Donati, L. & Unser, M. CryoGAN: a new reconstruction paradigm for single-particle cryo-EM via deep adversarial learning. *IEEE Trans. Comput. Imaging* **7**, 759–774 (2021).
154. Jumper, J. et al. Highly accurate protein structure prediction with AlphaFold. *Nature* **596**, 583–589 (2021).
155. Paul-Gilloteaux, P. et al. eC-CLEM: flexible multidimensional registration software for correlative microscopies. *Nat. Methods* **14**, 102–103 (2017).

Acknowledgements

We thank the Microscopy CORE Lab of the Maastricht MultiModal Molecular Imaging Institute of the Faculty of Health, Medicine and Life Sciences at Maastricht University for technical and scientific support. We thank M. Bárcena and S. Raunser and their co-authors for permission to modify and republish their figures. We thank H. Nguyen for editing the manuscript. We thank A. McDowall for critical reading of the manuscript. We acknowledge co-funding by the PPP Allowance made available by Health ~ Holland, Top Sector Life Sciences & Health, to stimulate public–private partnerships, under project number LHSM18067, as well as from the Netherlands Organisation for Scientific Research (NWO) in the framework of National Roadmap NEMI project number 184.034.014.

Competing interests

The University of Maastricht has filed patents, with R.B.G.R., C.L.-I. and P.J.P. as inventors, regarding vitrification devices. P.J.P. is a shareholder and chief scientific officer of the start-up CryoSol-World, which holds the licenses of these submitted patents (WO 2017/220750 and EP 3260839 B1). The other authors declare no competing interests.

Additional information

Correspondence and requests for materials should be addressed to Peter J. Peters.

Peer review information *Nature Methods* thanks the anonymous reviewers for their contribution to the peer review of this work. Primary Handling Editor: Rita Strack, in collaboration with the *Nature Methods* team.